RESEARCH ARTICLE

**ADVANCED
PHOTONICS
RESEARCH**
Open Access

www.adpr-journal.com

Semimetal–Monolayer Transition Metal Dichalcogenides Photodetectors for Wafer-Scale Broadband Photonics

Hon-Loen Sinn, Aravindh Kumar, Eric Pop, and Akm Newaz*

Atomically thin 2D transition metal dichalcogenides (TMDs), such as MoS_2, are promising candidates for nanoscale photonics because of strong light–matter interactions. However, Fermi-level pinning due to metal-induced gap states (MIGS) at the metal–monolayer (1L)-MoS_2 interface limits the application of optoelectronic devices based on conventional metals due to high contact resistance. On the other hand, a semimetal–TMD–semimetal device can overcome this limitation, where the MIGS are sufficiently suppressed allowing ohmic contacts. Herein, the optoelectronic performance of a bismuth–1L-MoS_2–bismuth device with ohmic electrical contacts and extraordinary optoelectronic properties is demonstrated. To address the wafer-scale production, full coverage 1L-MoS_2 grown by chemical vapor deposition. High photoresponsivity of 300 A W^{-1} at wavelength 400 nm measured at 77 K, which translates into an external quantum efficiency (EQE) ≈ 1000 or 10^5%, is measured. The 90% rise time of the devices at 77 K is 0.1 ms, suggesting they can operate at the speed of ≈ 10 kHz. High-performance broadband photodetector with spectral coverage ranging from 380 to 1000 nm is demonstrated. The combination of large-array device fabrication, high sensitivity, and high-speed response offers great potential for applications in photonics, including integrated optoelectronic circuits.

1. Introduction

Broadband photodetectors (BPD) with spectral coverage ranging from ultraviolet (UV) to near-infrared (NIR) range are at the heart of many applications ranging from high-capacity optical communication, night vision, biological analysis, environmental sensors, wide spectral switches, fire monitoring, and space exploration to radiation detection.[1–4] For example, near-infrared light detection capabilities enable image sensors combined with night vision systems.[5,6] Another important application is in optical data communication systems, in which the wide spectral bandwidth is used to increase optical data transmission capacity.[7]

Previous efforts have focused on developing photodetectors operating over a narrow wavelength spectrum, mostly due to the lack of proper materials which have could absorb incident photons over broad wavelength range with good optoelectronic conversion efficiency. Several approaches have been explored to develop efficient broadband photodetectors based on many nanomaterials and device designs.[1,4,8–11] For example, graphene show promises as an active material for broadband photodetector.[8,10] However, low photon absorption by monolayer graphene causes poor photoresponsivity. Another commonly investigated approach is to employ solution-processed organic halide perovskites.[4,12] However, solution process fabrication fundamentally imposes a limitation in reliably producing uniform films over a large area, or wafer-scale production. Another promising route to obtain broadband nanoscale photodetectors is to use atomically thin 2D semiconductors.

2D transition metal dichalcogenides (TMDs), such as MoS_2, provide an attractive platform for nanoscale photonics due to their atomic scale thickness, strong light–matter interaction, and favorable mechanical and electrical properties.[13–18] Moreover, wafer-scale growth of TMDs makes them promising candidates for future very large-scale integration (VLSI).[19–21]

Photons impinging on a monolayer TMD (1L-TMD) will produce direct bandgap optical transitions, also known as the A and B transitions.[13–18] In addition, there is also a pair of van Hove

H.-L. Sinn, A. Newaz
Department of Physics and Astronomy
San Francisco State University
San Francisco, CA 94132, USA
E-mail: akmnewaz@sfsu.edu

The ORCID identification number(s) for the author(s) of this article can be found under https://doi.org/10.1002/adpr.202300029.

A. Kumar, E. Pop
Department of Electrical Engineering
Stanford University
Stanford, CA 94305, USA

E. Pop
Department of Materials Science and Engineering
Stanford University
Stanford, CA 94305, USA

E. Pop
Precourt Institute for Energy
Stanford University
Stanford, CA 94305, USA

**ADVANCED
SCIENCE NEWS**

www.advancedsciencenews.com

**ADVANCED
PHOTONICS
RESEARCH**

www.adpr-journal.com

singularity (vHS)-assisted excitonic transitions (referred to as C[22] and D peaks[23]) in the UV regime $\approx$3–4 eV.[22] These excitons cause extraordinarily high photon absorption of 1L-TMDs ($\approx$40% for 1L-MoS$_2$[24–26]). It has been reported that the radiative lifetime of A- and B-excitons is few picoseconds.[25,27] The vHS excitons form within the continuum of the quasiparticle state, i.e., above the band edge, and decay spontaneously.[22] Due to spontaneous decay, the lifetime of the C-/D-excitons is also short ($\tau_C = 0.4$ ns).[28] High absorption and shorter lifetime of the excitons create an opportunity to develop an efficient and fast nanoscale broadband photodetector.

However, when a metal contact (e.g., Au) is evaporated on a 2D molybdenum disulfide (MoS$_2$) to prepare the metal contact, interface defects are created that pin the Fermi level near the conduction band, known as metal-induced gap states (MIGS). The formation of MIGS at the metal–semiconductor interface causes a Schottky barrier, which leads to high contact resistance, nonlinear current–voltage (I–V) characteristics, and poor current delivery capability.[29–31] All these factors limit the use of TMDs as next-generation photonic devices.

To unpin the Femi level, many efforts have been attempted, including indium metal contacts,[32,33] atomically flat Au metals,[34] and via contacts.[35] Recently, it has been reported that a semimetal–TMD–semimetal (STMDS) lateral device overcomes this limitation, where the MIGS are sufficiently suppressed, creating ohmic contacts with ultralow contact resistance.[36,37] By using semimetals (e.g., Bi, Sn, etc.) as the contact materials, Shen et al. and Kumar et al. demonstrated ohmic contacts with resistance as low as 123 Ω μm for Bi/1L-MoS$_2$/Bi and 270 Ω μm for Sn/Au alloy-MoS$_2$-Sn/Au alloy devices at room temperatures, respectively.[36,37]

The principal mechanism of MIGS suppression is that a semimetal has a near-zero density of states (DOS) at the Fermi level.[36] Hence, if the Fermi level of a semimetal is close to the conduction band minimum of a semiconductor, the MIGS from the conduction band are greatly reduced. This new semimetal/TMD contact technology may pave the way toward obtaining high-performance monolayer transistors that are on-par with the current silicon semiconductors technology and will allow extending Moore's law.

As STMDS demonstrates ultralow contact resistance, STMDS may demonstrate extraordinary optoelectrical performances and find a wide range of applications in next-generation device applications. Moreover, this semimetal/TMD-based technology will allow us to fabricate dense nanoscale optoelectrical devices directly into TMD-based VLSI electronic circuits. However, the optoelectronic properties of this new type of STMDS devices have not been reported yet. To the best of our knowledge, we present here the optoelectronic properties of an STMDS device for the first time.

In this work, we demonstrate the optoelectronic properties of an STMDS device based on bismuth (Bi)–1L-MoS$_2$–Bi photodetector devices. For wafer-scale applications of STMDS, full-coverage growth of 1L-TMDs is critical. To address this, we grew 1L-MoS$_2$ by solid-source chemical vapor deposition (CVD). We measured a high photoresponsivity of 300 A W^{-1} near the edge of the UV regime ($\approx$400 nm) at 77 K, which translates into an external quantum efficiency (EQE) $\approx$1000 or 10^5%. By measuring the photocurrent spectroscopy, we found that our devices
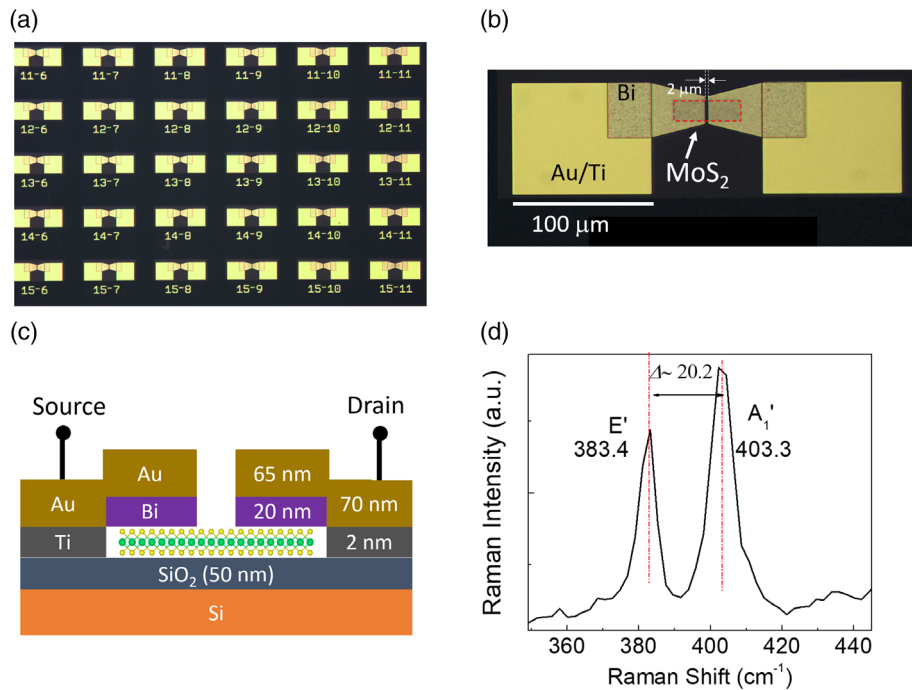
are most sensitive in the UV range and also have excellent broadband photoresponsivity with spectral coverage from 380 to 1000 nm. We have found that the 90% rise time and fall time of our devices is 0.1 ms, which suggests they could operate at the speed of $\approx$10 kHz.

2. Results and Discussion

We fabricated the TMD devices on SiO$_2$/undoped Si wafers. We selected an undoped Si wafer, obtained from a commercial vendor (University Wafer Inc.), to reduce the photogating effect, which arises due to the accumulation of the photogenerated carrier at the interface between SiO$_2$ and Si that gates the TMD electrostatically.[22,38,39] The surface crystal orientation of the undoped wafer was <100> and the resistivity of the wafer was >20 000 Ω cm. A 50 nm-thick SiO$_2$ was grown thermally, followed by growing monolayer MoS$_2$ by a solid-source CVD technique. A detailed description of the TMD layer preparation is available in the work by Smithe et al.[40,41] The optical image of an array of devices is shown in **Figure 1**a. The blown-up view of one device is shown in Figure 1b. A rectangular strip of 1L-MoS$_2$ of size 20 μm $\times$ 50 μm was patterned using optical lithography followed by O$_2$ plasma etching. The red-dashed line rectangle in Figure 1b shows the strip of 1L-MoS$_2$. Next, a semimetal (bismuth (Bi)) contact was formed by using optical lithography followed by electron beam (e-beam) evaporation. To avoid oxidation (Bi$_2$O$_3$), we deposited 65 nm of Au on top of Bi before we removed the sample from the evaporator (see Figure 1c). Moreover, it has been reported by Shen et al. that Bi$_2$O$_3$ does not form at the Bi/1L-MoS$_2$ interface during the Bi evaporation.[36]

Finally, large square wire-bonding contact pads (size: 100 μm $\times$ 100 μm) were prepared using optical lithography followed by thermal evaporation of Ti (2 nm) and Au (70 nm). The thicknesses of different components of a device are shown in Figure 1c. The monolayer nature of the film was confirmed by Raman spectroscopy measured at room temperature using a homemade system. Confocal micro-Raman measurements were performed after completing the device fabrication. A 100$\times$ objective lens with a numerical aperture of 0.85 was used. The excitation source was a 532 nm laser (2.33 eV) with an optical power of $\approx$500 μW. The Raman spectrum of a sample is shown in Figure 1d, revealing two signature peaks ($E' = 383.4$ cm^{-1} and $A'_1 = 403.3$ cm^{-1}) of 1L-MoS$_2$. The gap between the Raman peaks is $\Delta = 20.2$ cm^{-1}, which confirms that the sample is 1L-MoS$_2$.[42]

To study the temperature-dependent electrical and optoelectronic properties of an STMDS sample, we mounted the samples inside a microscopy cryostat (Janis Research, ST-500) equipped with electrical feedthrough for electro-optical measurements. The cryostat was coupled with an Olympus microscope equipped with a long-working distance objective (magnification 40$\times$). For wavelength-resolved measurements, we used a broadband light source (tungsten–halogen lamp) coupled to a double-grating monochromator (Acton Spectra Pro SP-2150i). The photocurrent was measured by employing the lock-in techniques.[43] The optical beam was modulated by an optical chopper ($f = 79$ Hz). The optical power on the sample was determined using a well-calibrated Si p–i–n photodetector (Hamamatsu S1223).

**ADVANCED
SCIENCE NEWS**

www.advancedsciencenews.com

**ADVANCED
PHOTONICS
RESEARCH**
Open Access

www.adpr-journal.com

Figure 1. Device characteristics. a) Optical image of an array of devices. b) Zoomed-in image of a single device. First, full-area coverage of monolayer MoS_2 was grown by solid-source CVD. The sample strips were prepared by optical lithography followed by oxygen plasma etching (red-dashed line rectangle). c) The device cross-section is shown schematically. d) Raman spectroscopy from the monolayer MoS_2 sample. The presence of two peaks (E' and A_1') confirm the monolayer nature of CVD-grown MoS_2. The excitation laser source was 532 nm.

We measured the electrical transport properties of the sample at different temperatures from 80 to 290 K, as shown in **Figure 2**. We measured the current using a programmable source meter (Keithley 2400) connected to a current preamplifier (Stanford Research SR570). The voltage signal from the current amplifier was measured by using a digital multimeter (Keithley 2000).

We studied a total of six devices, all of which showed similar results. The current–voltage (I–V) at different temperatures from 80 to 290 K is shown in Figure 2a. We observed that the I–V curves demonstrate very linear behavior near zero voltage, which

suggests that MIGS are suppressed and the contacts are Ohmic in nature. The resistance at different temperatures from 80 to 290 K at every 30 K step is shown in Figure 2b. The temperature dependence of the resistance demonstrates very semiconductor-like behavior. We note that the contact resistance also changes as we increase the temperature.

The Schottky barrier can be determined from the temperature-dependent I–V characteristics. The current (I) through an atomically thin 2D 1L-MoS_2 is governed by the 2D thermionic emission equation,[44] which employs a reduced $T^{1.5}$ power
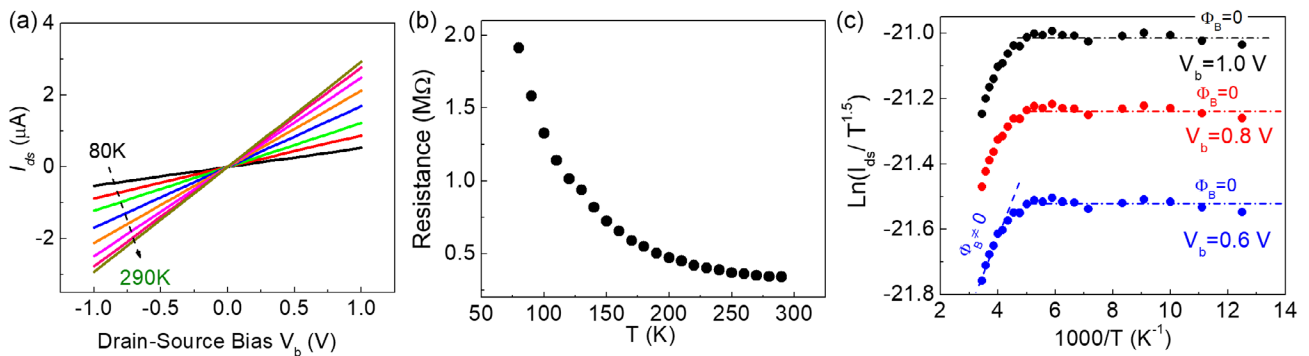
Figure 2. Electrical transport properties of a device. a) Current–voltage (I–V) curve of a device at different temperature from 80 to 290 K at every 30 K steps. The I–V curves were measured in the dark. The I–V curve shows excellent linear behavior. b) The resistance as a function of temperature. The resistance was measured from the slope of the I–V curves shown in (a). c) Determination of the Schottky barrier for different source-drain bias voltage (V_b). The Schottky barrier height vanishes at temperatures below 180 K. The nonzero slope in the plot (shown by blue dashed line for $V_b = 0.6$ V) suggests the formation of Schottky barrier at temperatures higher than 180 K. See the main text for details.

**ADVANCED
SCIENCE NEWS**

www.advancedsciencenews.com

**ADVANCED
PHOTONICS
RESEARCH**
Open Access

www.adpr-journal.com

law for 2D transport.[45] Our device behaves as two back-to-back Schottky diodes. In that case, most of the bias voltage drops on the reverse biased side.[46,47] The diode equation takes the form

$$I_{ds} = A_{2D}^* ST^{1.5} \exp\left[-\frac{q}{kT}\left(\Phi_B - \frac{V_b}{n}\right)\right] \times \left[1 - \exp\left(-\frac{qV_b}{kT}\right)\right]$$
(1)

where A_{2D}^* is the 2D equivalent Richardson constant, S is the contact area, n is the ideality factor, Φ_B is the Schottky barrier, k is the Boltzmann constant, q is the elementary charge, and V_b is the voltage applied between source–drain terminals. Now, it has been showed that when $\frac{qV_b}{kT} \geq 3$, the last term can be neglected[47] and the equation becomes

$$I_{ds} = A_{2D}^* ST^{1.5} \exp\left[-\frac{q}{kT}\left(\Phi_B - \frac{V_b}{n}\right)\right]$$
(2)

To determine the Schottky barrier, we utilize the Arrhenius plot, i.e., $\ln\left(\frac{I}{T^{1.5}}\right)$ versus $1000/T$, as shown in Figure 2c.[45,48] The slope of the plot will give $m = -\frac{q}{1000k}\left(\Phi_B - \frac{V_b}{n}\right)$. If we plot the slope as a function of V_b, the intercept of the new plot, $c_0 = -\frac{q\Phi_B}{1000k}$, will give a direct measure of the Schottky barrier height. We observed that the Arrhenius plots are horizontal below 180 K for different V_b as shown in Figure 2c, which means

that the slopes are zero or $m = 0$. Now, if we plot m versus V_b for temperatures below 180 K, the intercept of the plot c_0 will be zero, which means $\Phi_B = 0$. Hence, the Schottky barrier Φ_B of our devices vanishes below 180 K.

Note that the horizontal line (dashed-line in Figure 2c) separation between $V_b = 0.8$ V and $V_b = 0.6$ V is larger than the separation between $V_b = 0.8$ V and $V_b = 1.0$ V. This is originating as different $I_{ds}/T^{1.5}$ values are plotted in a logarithmic scale.

We propose a mechanism, similar to the mechanism proposed by Shen et al., for the vanishing of Schottky barrier in STMDS below $T \leq 180$ K.[36] We argue that the alignment of the Fermi level, near-zero DOS of a semimetal, and the bottom of the conduction-band minima is the reason for the formation of the ohmic contact at the interface.[36] We presented the DOS and the corresponding band structure schematically in the Supporting Information (S1). For a semimetal/semiconductor interface, the Fermi level is located at the near-zero DOS and aligned with the bottom of the conduction band. Hence, the MIGS from the conduction-band tail are heavily suppressed and the contacts become Schottky barrier free.

The optical and optoelectronic properties of a sample are shown in **Figure 3**. Photoluminescence spectrum was taken from the sample at room temperature with a 532 nm green laser and is shown in Figure 3a. We observed two peaks at 675 and 620 nm, which correspond to the A- and B-excitons in 1L-MoS$_2$,[22,49,50] confirming that our samples are of monolayer nature.
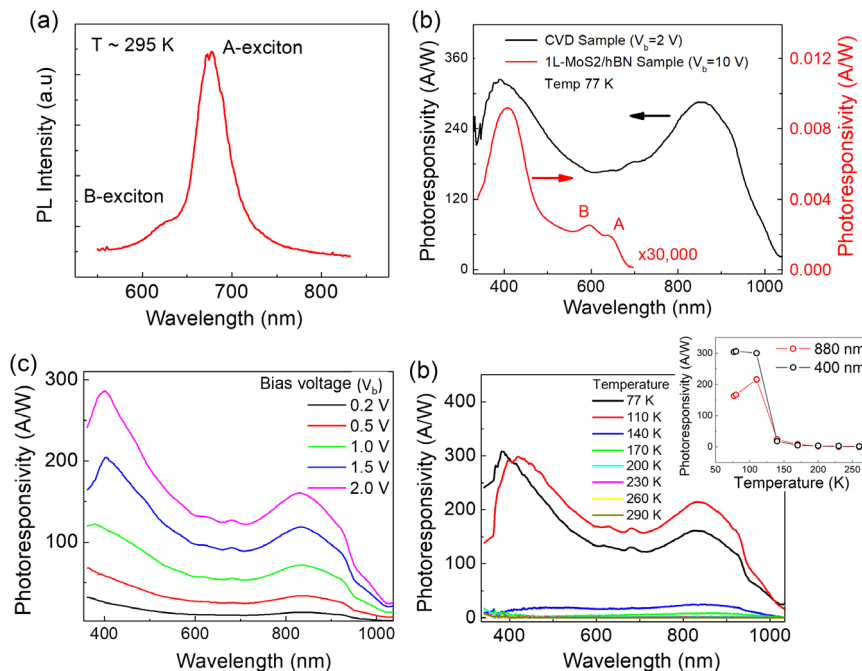
Figure 3. Optical and optoelectrical properties of a Bi–MoS₂–Bi device. a) Photoluminescence spectrum from a 1L-MoS₂ sample measured at room temperature. The excitation laser wavelength was 532 nm. Two neutral exciton peaks, A- and B-peaks, appear at 675 and 620 nm, respectively. b) Photoresponsivity (current per unit light power) of the sample (black solid line) at different wavelength. The red solid line is the photocurrent spectroscopy from a monolayer Au–MoS₂–Au sample on a glass substrate encapsulated by hBN. The photoresponsivity in the Au–1L-MoS₂–Au is 30 000 smaller than that from our Bi–MoS₂–Bi sample. Two peaks at 650 and 590 nm in the photoresponsivity spectrum of Au–1L-MoS₂–Au sample are due to the A- and B-excitons and are marked by A and B, respectively. c) Photoresponsivity of a sample at different bias voltages measured at 77 K. We found a linear behavior as we increased the bias voltage. d) Photoresponsivity of a sample at different temperature. The photoresponsivity vanishes as the temperature is increased. Inset: The amplitude of the photocurrent peak in the infrared region (red circle line, wavelength ≈880 nm) and UV edge (black circle line, ≈400 nm) at different temperatures.

We measured photocurrent using two different types of optical sources: 1) lasers (wavelength 405 and 650 nm) and 2) a broadband tungsten–halogen thermal source. In atomically thin 2D TMD-based photodetectors, the photocurrent originates from two main mechanisms: 1) the photoconductive effect, where the photogenerated electron–hole pairs increase the carrier density and the electrical conductivity; and 2) the photogating effect, where the photogenerated carriers filled the localized trap states and cause a shift of the Fermi energy.[51–57] We have probed the photoconductive mechanisms in our devices by measuring photocurrent with varying light power, bias voltages, and laser pulse width. Our measurements show that photogating is the dominant mechanism in our devices.

To understand the photocurrent mechanism, we determined the wavelength-resolved photoresponsivity (photocurrent per unit power of lights), R_λ, of the sample for a wide range of wavelengths from the edge of UV ($\lambda = 380$ nm) to near-infrared ($\lambda = 1050$ nm). Figure 3b shows the photoresponsivity of an STMDS sample measured at 77 K. The light power on the sample was calibrated by a Si p–i–n photodetector (Hamamatsu S1223). We measured the scanning photocurrent image of the sample to map the region of photocurrent contribution and found zero photocurrent outside our sample (see Supporting Information).

We observed three important features. First, we observed one peak at 380 nm. We attributed this peak to the van Hove singularity exciton, which also causes the highest absorption of photons.[22] Second, the photocurrent peaks due to A- and B-excitons are not visible in the spectrum. We attribute this due to the photogating effect which is the main mechanism of the photocurrent generation in our STMDS devices. There are two competing photocurrents in our devices. One photocurrent is originating from the exciton dissociations[22] and the second photocurrent is originating from the photogating.[58] As the photocurrent due to photogating is several orders of magnitude higher than the photocurrent due to exciton dissociation, the signatures of A- and B-exciton peaks do not appear in the photocurrent spectrum. We observed peaks in the photocurrent spectrum due to the A- and B-excitons for samples that were grown following the similar solid-source CVD method and were prepared on a quartz crystal substrate (see Supporting Information). We electrically connected the sample by Ag/Au metal layers and we used a quartz substrate to remove the photogating effect completely.[42] When the photogating effect is absent, as exciton dissociation is the dominant photocurrent mechanism and the exciton-related peaks appear in the photocurrent spectrum of Au/Ag/1L-MoS$_2$/Ag/Au devices (see Supporting Information). Also, we measured that the photoresponsivity in Au/Ag/1L-MoS$_2$/Ag/Au devices is six orders of magnitude lower than that in MoS$_2$/Bi devices (see Supporting Information).

Finally, we also observed a photoresponsivity peak in the infrared region ($\approx$880 nm at 77 K). To understand the origin of the infrared peak, we studied the absorption and photocurrent in the infrared regime of an Ag/Au/1L-MoS$_2$/Ag/Au device (see Supporting Information). If the photogating is absent in a device, the photocurrent is proportional to the absorption coefficient. Hence, the photoresponsivity spectrum in our Au/Ag/1L-MoS$_2$/Ag/Au sample on a quartz substrate is proportional to the absorption spectrum. We measured zero photocurrent in those Au/Ag/1L-MoS$_2$/Ag/Au devices for wavelengths 700–1100 nm (see Supporting Information), which suggests that the infrared peak in the Bi/1L-MoS$_2$/Bi sample is not due to any intrinsic properties or defects in the CVD grown 1L-MoS$_2$. We propose that the infrared peak is originating due to the Si/SiO$_2$/MoS$_2$ heterojunction. Indeed, the silicon photodiode demonstrates a responsivity peak around 900 nm.[59] Moreover, similar infrared peak in the photocurrent detectivity has been reported for graphene–Si heterojunction.[10]
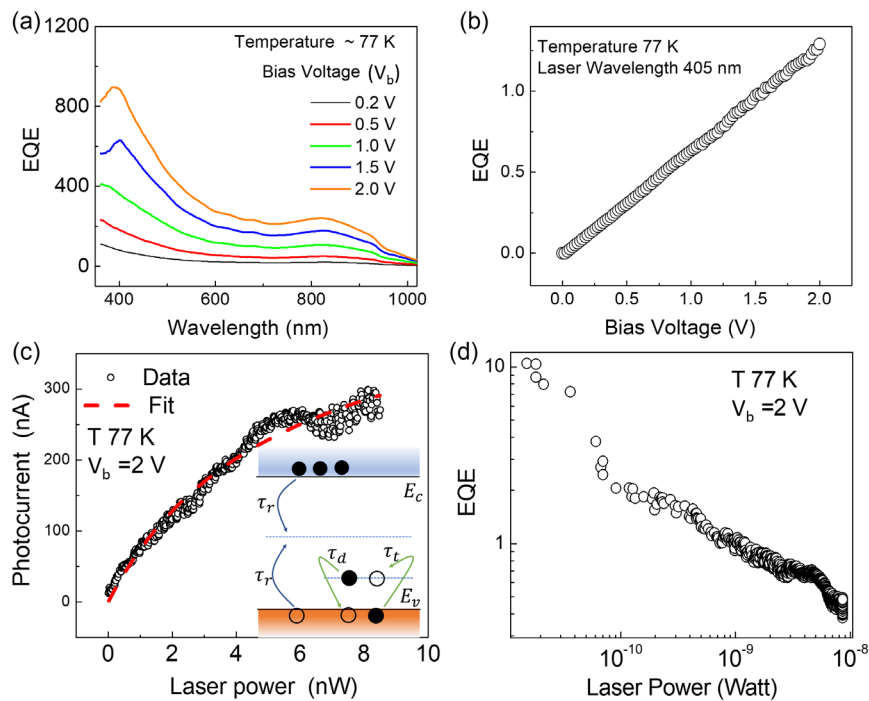
Now, we present detailed experimental results supporting the photogating mechanism in STMDS devices. To compare the photocurrent spectrum with conventional microexfoliated TMDs, we also studied the photocurrent spectroscopy of a high-quality 1L-MoS$_2$ sample encapsulated by a thin hexagonal boron nitride (hBN) flake as shown in Figure 3b (red line). The samples were fabricated on a glass substrate using the dry transfer technique and were electrically connected to a pre-patterned Au electrode. For detailed results on fabrication and photocurrent spectroscopy of exfoliated 1L-MoS$_2$, we guide the reader to our previous publications by Benson et al.[60] The right axis in Figure 3b presents the photoresponsivity from the 1L-MoS$_2$ sample. The photoresponsivity in our STMDS samples is $\approx$30 000 times larger than that from an exfoliated 1L-MoS$_2$ sample, which suggests extraordinarily high photocurrent in STMDS device. The two peaks at 650 and 590 nm in the photoresponsivity spectrum of 1L-MoS$_2$/hBN sample in Figure 3b are due to A- and B-excitons.

To understand the electric field-dependent photocurrent, we also studied photocurrent spectra for different bias voltages as shown in Figure 3c. We see that photocurrent increases linearly as we increase the bias voltage. Figure 3d presents the temperature dependence property of the photocurrent spectrum over a wide range of temperatures from 80 to 298 K. We observe that photocurrent decreases sharply at temperatures higher than 120 K and almost disappears near room temperature ($T \geq 250$ K).

To determine the temperature-dependent behavior of photocurrent, we measured the amplitude of the photocurrent peak in the infrared ($\approx$880 nm) and UV edge ($\approx$400 nm) at different temperatures, as shown in the inset of Figure 3d. We observed that the photocurrent increases as we raise the temperature from 77 K and peaked at $\approx$110 K. Similar behavior of temperature-dependent photocurrent was observed in MoS$_2$[61] and natural van der Waals heterostructure, Franckeite.[43]

The variation of photocurrent due to temperature originates from two main factors: 1) change of contact resistance and 2) trap states. We propose here that at low temperature ($T \leq 110$ K), the trap states originate from valence-band-contributed MIGS and the numbers of photogenerated carriers are higher than the number of trap states (also acting as the recombination centers). As we increase the temperature from 77 K ($77K \leq T \leq 110$ K), the contact resistance decreases, which increases the photocurrent. At temperature higher than 110 K ($T \geq 110$), we propose that photocurrent reduces for two reasons: 1) localized defect states become extended defects in 1L-MoS$_2$[62] and 2) the number of photogenerated carriers becomes smaller than the number of trap states.[61]

To determine the photodetector performance, we calculated the EQE, which is defined as a ratio of the number of electrons

**ADVANCED
SCIENCE NEWS**

www.advancedsciencenews.com

**ADVANCED
PHOTONICS
RESEARCH**
Open Access

www.adpr-journal.com

Figure 4. Measurements of EQE, which is defined as the number of electrons for one photon. a) EQE of a sample at different wavelength. We have observed very high EQE. The highest efficiency was observed for UV photons ($\approx$400 nm). Note that in the EQE calculation, we have not included the photon absorption efficiency. If we include the photon absorption efficiency, the EQE will be an order of magnitude higher. b) The measurement of EQE as a function of bias voltage. Here, we used a 405 nm laser. To improve the signal, we have used a high-power laser beam; that is why EQE is lower for this measurement. c) Photocurrent as a function of a 405 nm laser power measured at 77 K. The bias voltage was 2 V. Inset: Simplified energy band diagram that shows the main features of the charge trapping and detrapping model. The valence band trail is approximated by a discrete distribution of hole traps with density D_t (occupation of traps p_t). The holes are trapping into the states and detrapping out of the sates with a rate $1/\tau_t$ and $1/\tau_d$, respectively. d) EQE as a function of the laser power. We see that EQE decreases logarithmically as we increase the power, which is a clear sign that the high EQE is originating from the photogating effect as describe above.

in the external circuit to the number of incident photons. **Figure 4**a presents EQE for different bias voltage (V_b), which is connected to photoresponsivity R_λ by $EQE = \frac{R_\lambda}{\lambda} \times 1240$, where R_λ is the responsivity in A W^{-1} and λ is the wavelength in nm. We observed an EQE of 1000 or 10^5% at 77 K for a bias of 2 V. Note that high photoresponsivity was reported for a 1L-MoS$_2$ phototransistor sample before, where the samples are gated by a very large gate voltage.[58] To the best of our knowledge, we observed the highest EQE values for a two-terminal device without requiring any gate voltage, which can be beneficial for many imaging applications. This extremely large EQE suggests that our STMDS device has great potential for an extremely sensitive broadband photodetector.

To understand the origin of this extraordinary EQE, we measured photoresponsivity behavior of STMDS devices as a function of bias voltage and laser power. Figure 4b shows EQE as a function of bias voltage at 77 K while the device was illuminated by a 405 nm laser. The lower EQE value in Figure 4b is due to the high laser power used in this measurement. We observed a very linear behavior of EQE as a function of the bias voltage, which suggests that the gain mechanism is related to the photogating of the sample. The vanishing of photocurrent or EQE at $V_b = 0$ indicates that photovoltaic effect,

which may occur for a semimetal/TMD interface,[63] does not contribute to any photocurrent in our devices. We attribute the absence of the photovoltaic effect to the absence of the Schottky barrier at the semimetal/MoS$_2$ interface. To determine the photoresponse mechanism further, we have conducted laser power-dependent photocurrent study as shown in Figure 4c.

Following the earlier literature,[51,57,64] we have analyzed our laser power-dependent data using the Hornbeck–Haynes model.[65,66] It has been demonstrated that the structural defects and disorder cause the band tail states or shallow trap states near the valence band and conduction band.[67–69] In addition to the shallow trap states, there also exists deep recombination centers, also known as midgap states, which cause nonradiative (Shockley–Read–Hall-type) recombination.[51,57] The physical mechanism is shown schematically in the inset of Figure 4c. For the n-doped 1L-MoS$_2$, only the hole traps near the valence band are relevant. The trapping and detrapping of the hole states occur with rate $1/\tau_t$ and $1/\tau_d$, respectively. If the filling of the trap states by photogenerated carrier causes the electrostatic gating, it will shift the Fermi energy and increase the electrical conduction. Using this model, the photogated current is given by (see Supporting Information for detail calculations)

$$I_{PC} = A \frac{1}{1 + \frac{B}{P_D}}$$ (3)

The two parameters A and B are given by

$$A = \frac{D_t C_g C_q}{e(C_g + C_q)} \frac{dV_b}{dV_g}; \qquad B = \frac{D_t hc}{\eta \lambda \tau_r} \left(\frac{\tau_t}{\tau_d} \right)$$ (4)

where D_t is the density of the localized traps, C_g is the geometrical capacitance, C_q is the quantum capacitance, V_g is the gate voltage, e is the electron charge, h is the Planck constant, λ is the excitation laser wavelength, and η is the absorption coefficient of 1-MoS$_2$. The laser power-dependent photocurrent is fitted with this model using A and B as the fitting parameter as shown in Figure 4c. We obtained excellent fitting of the experimental data confirming that photogating is the main mechanism in our devices. As we have used an undoped substrate, we could not determine the $\frac{dV_b}{dV_g}$ and the density of traps using the fitting parameters. Figure 4d presents EQE as a function of laser power measured at 77 K. Note that EQE decreases logarithmically as a function of laser power, which is also a signature of the photogating effect.[58]

Finally, we studied the time response of our devices at 77 K as shown in **Figure 5**. The devices were illuminated by a chopped laser ($f = 700$ Hz) and the signal was measured by an oscilloscope. The bias voltage of the devices was 2 V. The time response of the photocurrent for a single pulse is shown in Figure 5a. We observed that the 90% rise time of the photocurrent is 0.1 ms, i.e., the frequency response of the current devices is $\approx$10 kHz as shown in Figure 5a. By measuring photocurrent for a long time after terminating the laser illumination, we did not observe the presence of persistent photocurrent in our STMDS devices (see Supporting Information).

To understand the decay time of the photocurrent in the dark, we also studied time response as a function of V_b, laser power, and temperature T, as shown in Figure 5b–d. We observed that the decay time in the dark does not depend on temperature and the bias voltage as shown in Figure 5b,d, respectively. On the other hand, the decay of the photocurrent after cessation of laser excitation depends strongly on the laser power impinging on the device as shown in Figure 5c. The decay time was measured by fitting an exponential decay function ($I = I_0 e^{-t/\tau}$, where t is the time and τ is the decay constant). We observed that the decay constant decreases monotonically as we increase the laser power. This is also a signature of the photogating effect. At a lower intensity, the trap states remain unsaturated and dominate the photocurrent decay after the cessation of laser excitation. With increasing laser power, the trap states get saturated and do not dominate the photocurrent decay resulting in a much lower (i.e., faster) decay time. Similar property of decay time as a function of control gate voltage was reported for a 1L-MoS$_2$
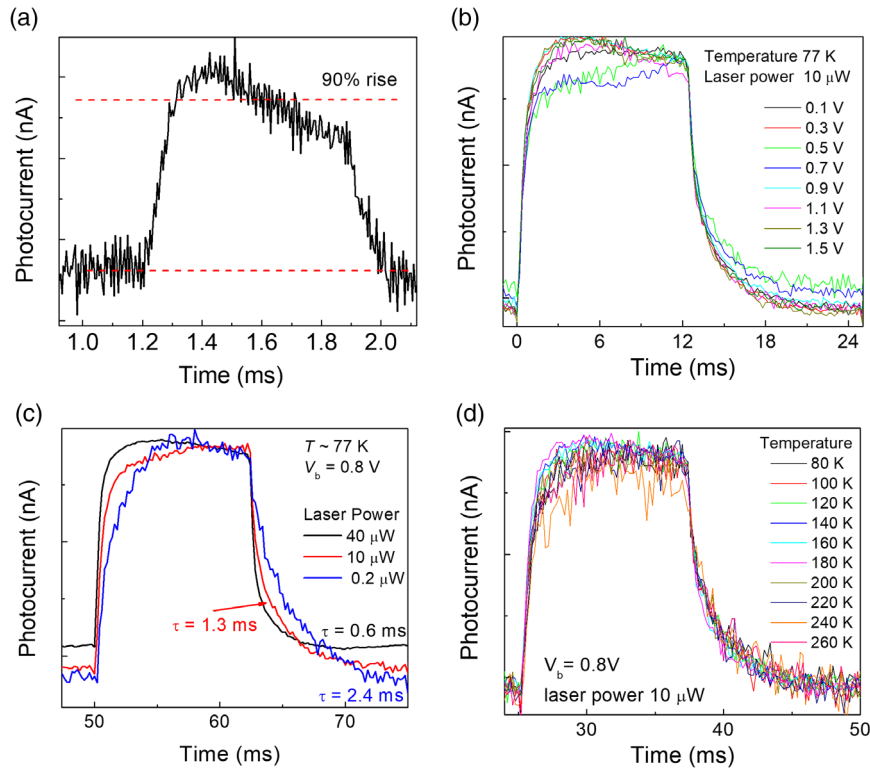
Figure 5. Time response of the device measured at 77 K. a) Time response of the device for a single laser pulse. We used a 405 nm laser modulated by a mechanical chopper ($f = 700$ Hz). We observed that a 90% rise time is 0.1 ms. b) Time response of the device for different V_b measured for a 10 μW laser power. No correlations between the decay time after the cessation of the laser and the bias voltage has been observed. c) Time response as a function of different laser power. The measured decay time increases as we increase the laser power. The determined decay time is marked next to the lines. d) Time response as a function of temperature. No correlations between the decay time after the cessation of the laser and the temperature has been observed.

**ADVANCED
SCIENCE NEWS**

www.advancedsciencenews.com

**ADVANCED
PHOTONICS
RESEARCH**

www.adpr-journal.com

phototransistor.[56] Hence, all our results consistently suggest that the high EQE observed in our devices is originating from the photogating effect in 1L-MoS$_2$ or at the interface between 1L-MoS$_2$ and the oxide layer. Also, we investigated the time response of the sample using a red laser ($\approx$650 nm). The details of this result are presented in the Supporting Information. We found that the 90% rise time of the photocurrent is 0.4 ms and the photocurrent decay becomes slower as the laser power is increased.

An interesting photodetector device structure would be to investigate devices with Bi/1L-MoS$_2$/Au contacts, such that one contact is Ohmic and the other is a Schottky contact. We plan to extend our investigation by studying those devices and present the result in a future publication.

To tune the EQE by using electrostatic gating, we measured photocurrent EQE of our STMDS devices by applying a back-gate voltage. We used Silver Conductive Paint or Silver Colloidal Suspension on the back side of the Si substrate to prepare a metallic gate. The circuit configuration of an STMDS device with a back-gate is shown in **Figure 6**a, which is effectively working as a phototransistor. The application of a back-gate voltage changes the doping concentration near the sample, which modifies the photoresponsivity. Figure 4b shows that EQE increases as we apply a negative back-gate voltage. We argue that the application of a negative gate voltage lowers the Fermi level, which makes more trap states available to the photogenerated carrier and increases EQE. We found that EQE can be enhanced significantly

by electrostatically doping the samples as shown in Figure 6b. The EQE was enhanced by 4 times (EQE$_{Max}$ = 4000) when the back-gate voltage is -6 V. This also confirms that the high EQE observed in our devices is due to photogating effect.

We present the EQE plots for six different devices, as shown in Figure 6c, to demonstrate the device performance variation. All the measurements were conducted under the same optical and electrical settings at 77 K. We found that the average EQE values for all devices at 400 nm is 1200 $\pm$ 430. Hence, the maximum responsivity at $\lambda = 400$ nm varies by $\approx$50% from the average values as shown in Figure 6c.

As our STMDS devices work the best around 400 nm wavelength photons, we will discuss the figure of merit of our photodetector compared to other solid-state UV photodetectors reported in the literature. The responsivity and the response time of different solid-state UV photodetectors are shown in Figure 6d, which are obtained from the review article by Alaie et al.[70] The responsivity and the response-time data for multilayer MoS$_2$/Au, CVD MoS$_2$/Au and exfoliated 1L, exfoliated MoS$_2$/Au, and β-Ge$_2$O$_3$ devices were reported by Zhang et al.,[71] Yore et al.,[42] Furchi et al.,[51] and Arora et al.,[72] respectively. Figure 6b clearly shows that our semimetal–TMD-based UV photodetector demonstrates superior performance. Hence, such a semimetal–TMD–semimetal photodetector possesses a true potential for next-generation solid-state photodetectors.
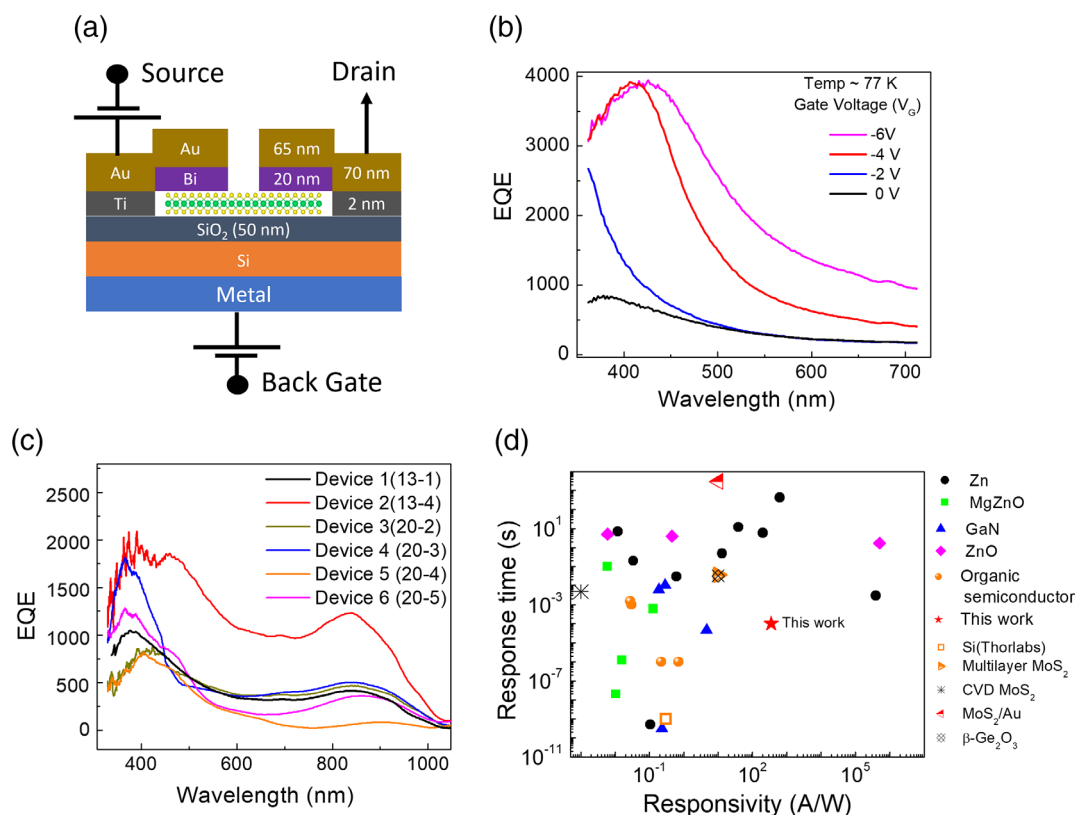
Figure 6. a) Circuit configuration of an STMDS device as a phototransistor. This circuit configuration was used to study the electrostatic gating effect on photocurrent. b) EQE of the device for back-gate voltages 0 V (black), -2 V (blue), -4 V (red), and -6 V (magenta). c) EQE of six devices measured at 77 K with a bias voltage $V_b = 2$ V. d) Responsivity values versus response time plot for different type of solid-state UV photodetectors reported in the literature. See main text for the references.

**ADVANCED
SCIENCE NEWS**

www.advancedsciencenews.com

**ADVANCED
PHOTONICS
RESEARCH**

www.adpr-journal.com

Because of outstanding structural and mechanical properties,[73] monolayer TMDs can be easily fabricated on Si-based photonic structures for many applications ranging from covert communications and biological analysis to fire monitoring and UV astronomy. Fast response makes STMDS devices attractive for optical to electrical interconnects, which may find applications in communication devices.[74,75] High EQE values of STMDS make them attractive for low-light-level detections, such as single photon applications or photon-starved UV astronomy.

3. Conclusion

In conclusion, we demonstrated large array fabrication of fast and ultrasensitive photodetectors based on CVD-grown 1L-MoS$_2$ electrically connected by Bi semimetal that forms an ohmic contact at the interfaces and demonstrates efficient photodetection. We determined several important figures of merits for our devices: responsivity, EQE, time response, and scalability. Our results yield a fundamental understanding of semimetal–TMD–semimetal devices and will provide important information to develop next-generation TMD-based wafer-scale nanophotonic devices.

Supporting Information

Supporting Information is available from the Wiley Online Library or from the author.

Conflict of Interest

The authors declare no conflict of interest.

Data Availability Statement

The data that support the findings of this study are available from the corresponding author upon reasonable request.

[1] D.-S. Um, Y. Lee, S. Lim, J. Park, W.-C. Yen, Y.-L. Chueh, H-J. Kim, H. Ko, *ACS Appl. Mater. Interfaces* **2016**, *8*, 26105.

[2] F. Omnes, E. Monroy, E. Munoz, J. L. Reverchon, *Proc. of SPIE*, Vol. *6473* **2007**, p. 64730E.

[3] Y. H. Zhou, H. N. An, C. Gao, Z. Q. Zheng, B. Wang, *Mater. Lett.* **2019**, *237*, 298.

[4] X. Hu, X. Zhang, L. Liang, J. Bao, S. Li, W. Yang, Y. Xie, *Adv. Funct. Mater.* **2014**, *24*, 7373.

[5] B. Fowler, C. Liu, S. Mims, J. Balicki, W. Li, H. Do, P. Vu, *SPIE Proc.* Vol. *7298* DCS, SPIE, **2009**.

[6] E. A. Essock, M. J. Sinai, J. S. McCarley, W. K. Krebs, J. K. DeFord, *Hum. Factors* **1999**, *41*, 438.

[7] A. Dutta, M. S. Islam, Optics East 2005 **2005**, 6014, https://doi.org/10.1117/12.634119.

[8] C.-H. Liu, Y.-C. Chang, T. B. Norris, Z. Zhong, *Nat. Nanotechnol.* **2014**, *9*, 273.

[9] E. H. Sargent, *Adv. Mater.* **2008**, *20*, 3958.

[10] X. An, F. Liu, Y. J. Jung, S. Kar, *Nano Lett.* **2013**, *13*, 909.

[11] M. Buscema, D. J. Groenendijk, S. I. Blanter, G. A. Steele, H. S. J. Van Der Zant, A. Castellanos-Gomez, *Nano Lett.* **2014**, *14*, 3347.

[12] C. Li, H. Wang, F. Wang, T. Li, M. Xu, H. Wang, Z. Wang, X. Zhan, W. Hu, L. Shen, *Light Sci. Appl.* **2020**, *9*, 31.

[13] Q. H. Wang, K. Kalantar-Zadeh, A. Kis, J. N. Coleman, M. S. Strano, *Nat. Nano* **2012**, *7*, 699.

[14] K. F. Mak, J. Shan, *Nat. Photonics* **2016**, *10*, 216.

[15] F. Xia, H. Wang, D. Xiao, M. Dubey, A. Ramasubramaniam, *Nat. Photonics* **2014**, *8*, 899.

[16] X. Duan, C. Wang, A. Pan, R. Yu, X. Duan, *Chem. Soc. Rev.* **2015**, *44*, 8859.

[17] D. Jariwala, V. K. Sangwan, L. J. Lauhon, T. J. Marks, M. C. Hersam, *ACS Nano* **2014**, *8*, 1102.

[18] S. Manzeli, D. Ovchinnikov, D. Pasquier, O. V. Yazyev, A. Kis, *Nat. Rev. Mater.* **2017**, *2*, 17033.

[19] A. Sebastian, R. Pendurthi, T. H. Choudhury, J. M. Redwing, S. Das, *Nat. Commun.* **2021**, *12*, 693.

[20] H. Yu, M. Liao, W. Zhao, G. Liu, X. J. Zhou, Z. Wei, X. Xu, K. Liu, Z. Hu, K. Deng, S. Zhou, J.-A. Shi, L. Gu, C. Shen, T. Zhang, L. Du, L. Xie, J. Zhu, W. Chen, R. Yang, D. Shi, G. Zhang, *ACS Nano* **2017**, *11*, 12001.

[21] T. Li, W. Guo, L. Ma, W. Li, Z. Yu, Z. Han, S. Gao, L. Liu, D. Fan, Z. Wang, Y. Yang, W. Lin, Z. Luo, X. Chen, N. Dai, X. Tu, D. Pan, Y. Yao, P. Wang, Y. Nie, J. Wang, Y. Shi, X. Wang, *Nat. Nanotechnol.* **2021**, *16*, 1201.

[22] A. R. Klots, A. K. M. Newaz, B. Wang, D. Prasai, H. Krzyzanowska, J. Lin, D. Caudel, N. J. Ghimire, J. Yan, B. L. Ivanov, K. A. Velizhanin, A. Burger, D. G. Mandrus, N. H. Tolk, S. T. Pantelides, K. I. Bolotin, *Sci. Rep.* **2014**, *4*, 6608.

[23] D. Dumcenco, D. Ovchinnikov, K. Marinov, P. Lazić, M. Gibertini, N. Marzari, O. L. Sanchez, Y.-C. Kung, D. Krasnozhon, M.-W. Chen, S. Bertolazzi, P. Gillet, A. Fontcuberta, I. Morral, A. Radenovic, A. Kis, *ACS Nano* **2015**, *9*, 4611.

[24] D. Y. Qiu, F. H. da Jornada, S. G. Louie, *Phys. Rev. Lett.* **2013**, *111*, 216805.

[25] H. Wang, C. Zhang, W. Chan, C. Manolatou, S. Tiwari, F. Rana, *Phys. Rev. B* **2016**, *93*, 045407.

[26] L. Britnell, R. M. Ribeiro, A. Eckmann, R. Jalil, B. D. Belle, A. Mishchenko, Y.-J. Kim, R. V. Gorbachev, T. Georgiou, S. V. Morozov, A. N. Grigorenko, A. K. Geim, C. Casiraghi, A. H. Castro. Neto, K. S. Novoselov, *Science* **2013**, *340*, 1311.

[27] M. Palummo, M. Bernardi, J. C. Grossman, *Nano Lett.* **2015**, *15*, 2794.

[28] L. Wang, Z. Wang, H.-Y. Wang, G. Grinblat, Y.-L. Huang, D. Wang, X.-H. Ye, X.-B. Li, Q. Bao, A.-S. Wee, S. A. Maier, Q.-D. Chen, M.-L. Zhong, C.-W. Qiu, H.-B. Sun, *Nat. Commun.* **2017**, *8*, 13906.

[29] J. Tersoff, *Phys. Rev. B* **1985**, *32*, 6968.

[30] C. Tejedor, F. Flores, E. Louis, *J. Phys. C: Solid State Phys.* **1977**, *10*, 2163.

[31] W. Monch, *Rep. Prog. Phys.* **1990**, *53*, 221.

[32] Y. Wang, J. C. Kim, R. J. Wu, J. Martinez, X. Song, J. Yang, F. Zhao, A. Mkhoyan, H. Y. Jeong, M. Chhowalla, *Nature* **2019**, *568*, 70.

[33] B.-K. Kim, T.-H. Kim, D.-H. Choi, H. Kim, K. Watanabe, T. Taniguchi, H. Rho, J.-J. Kim, Y.-H. Kim, M.-H. Bae, *npj 2D Mater. Appl.* **2021**, *5*, 9.

[34] Y. Liu, J. Guo, E. Zhu, L. Liao, S.-J. Lee, M. Ding, I. Shakir, V. Gambin, Y. Huang, X. Duan, *Nature* **2018**, *557*, 696.

[35] E. J. Telford, A. Benyamini, D. Rhodes, D. Wang, Y. Jung, A. Zangiabadi, K. Watanabe, T. Taniguchi, S. Jia, K. Barmak, A. N. Pasupathy, C. R. Dean, J. Hone, *Nano Lett.* **2018**, *18*, 1416.

[36] P.-C. Shen, C. Su, Y. Lin, A.-S. Chou, C.-C. Cheng, J.-H. Park, M.-H. Chiu, A.-Y. Lu, H.-L. Tang, M. M. Tavakoli, G. Pitner, X. Ji, Z. Cai, N. Mao, J. Wang, V. Tung, J. Li, J. Bokor, A. Zettl, C.-I. Wu, T. Palacios, L.-J. Li, J. Kong, *Nature* **2021**, *593*, 211.

[37] A. Kumar, K. Schauble, K. M. Neilson, A. Tang, P. Ramesh, H.-S. P. Wong, E. Pop, K. Saraswat, *IEEE International Electron Devices Meeting (IEDM)*, IEEE, San Francisco, USA **2021**, pp. 7.3.1–7.3.4. https://doi.org/10.1109/IEDM19574.2021.9720609.

[38] M. Freitag, T. Low, F. Xia, P. Avouris, *Nat. Photonics* **2013**, *7*, 53.

[39] G. Konstantatos, M. Badioli, L. Gaudreau, J. Osmond, M. Bernechea, F. P. G. De Arquer, F. Gatti, F. H. L. Koppens, *Nat. Nano* **2012**, *7*, 363.

[40] K. K. H. Smithe, C. D. English, S. V. Suryavanshi, E. Pop, *Nano Lett.* **2018**, *18*, 4516.

[41] K. K. H. Smithe, C. D. English, S. V. Suryavanshi, E. Pop, *2D Mater.* **2017**, *4*, 011009.

[42] A. E. Yore, K. K. H. Smithe, S. Jha, K. Ray, E. Pop, A. K. M. Newaz, *Appl. Phys. Lett.* **2017**, *111*, 043110.

[43] K. Ray, A. E. Yore, T. Mou, S. Jha, K. K. H. Smithe, B. Wang, E. Pop, A. K. M. Newaz, *ACS Nano* **2017**, *11*, 6024.

[44] A. Anwar, B. Nabet, J. Culp, F. Castro, *J. Appl. Phys.* **1999**, *85*, 2663.

[45] W. Wang, Y. Liu, L. Tang, Y. Jin, T. Zhao, F. Xiu, *Sci. Rep.* **2014**, *4*, 6928.

[46] B. H. Moon, G. H. Han, H. Kim, H. Choi, J. J. Bae, J. Kim, Y. Jin, H. Y. Jeong, M.-K. Joo, Y. H. Lee, S. C. Lim, *ACS Appl. Mater. Interfaces* **2017**, *9*, 11240.

[47] M. Ahmetoglu, S. K. Akay, *Curr. Appl. Phys.* **2010**, *10*, 652.

[48] Q. Z. Liang, X. X. Yao, W. Wang, Y. Liu, C. P. Wong, *ACS Nano* **2011**, *5*, 2392.

[49] A. Splendiani, L. Sun, Y. Zhang, T. Li, J. Kim, C.-Y. Chim, G. Galli, F. Wang, *Nano Lett.* **2010**, *10*, 1271.

[50] K. F. Mak, C. Lee, J. Hone, J. Shan, T. F. Heinz, *Phys. Rev. Lett.* **2010**, *105*, 136805.

[51] M. M. Furchi, D. K. Polyushkin, A. Pospischil, T. Mueller, *Nano Lett.* **2014**, *14*, 6165.

[52] B. Miller, E. Parzinger, A. Vernickel, A. W. Holleitner, U. Wurstbauer, *Appl. Phys. Lett.* **2015**, *106*, 122103.

[53] J. O. Island, S. I. Blanter, M. Buscema, H. S. J. van der Zant, A. Castellanos-Gomez, *Nano Lett.* **2015**, *15*, 7853.

[54] H. Fang, W. Hu, *Adv. Sci.* **2017**, *4*, 1700323.

[55] H. Huang, J. Wang, W. Hu, L. Liao, P. Wang, X. Wang, F. Gong, Y. Chen, G. Wu, W. Luo, H. Shen, T. Lin, J. Sun, X. Meng, X. Chen, J. Chu, *Nanotechnology* **2016**, *27*, 445201.

[56] D. Kufer, G. Konstantatos, *Nano Lett.* **2015**, *15*, 7307.

[57] D. Vaquero, V. Clericò, J. Salvador-Sánchez, E. Díaz, F. Domínguez-Adame, L. Chico, Y. M. Meziani, E. Diez, J. Quereda, *Nanoscale* **2021**, *13*, 16156.

[58] O. Lopez-Sanchez, D. Lembke, M. Kayci, A. Radenovic, A. Kis, *Nat. Nanotechnol.* **2013**, *8*, 497.

[59] K. Mangold, J. A. Shaw, M. Vollmer, *Eur. J. Phys.* **2013**, *34*, S51.

[60] G. Benson, V. Zurdo Costa, N. Border, K. Yumigeta, M. Blei, S. Tongay, K. Watanabe, T. Taniguchi, A. Ichimura, S. Kc, T. Salavati-Fard, B. Wang, A. Newaz, *J. Phys. Chem. C* **2022**, *126*, 8667.

[61] S. Ghosh, A. Winchester, B. Muchharla, M. Wasala, S. Feng, A. L. Elias, M. B. M. Krishna, T. Harada, C. Chin, K. Dani, S. Kar, M. Terrones, S. Talapatra, *Sci. Rep.* **2015**, *5*, 11272.

[62] S. Chandan, S. Sarkar, B. Angadi, *Appl. Phys. Lett.* **2021**, *118*, 172105.

[63] M. Fontana, T. Deppe, A. K. Boyd, M. Rinzan, A. Y. Liu, M. Paranjape, P. Barbara, *Sci. Rep.* **2013**, *3*, 1634.

[64] D. Macdonald, A. Cuevas, *Appl. Phys. Lett.* **1999**, *74*, 1710.

[65] J. R. Haynes, J. A. Hornbeck, *Phys. Rev.* **1953**, *90*, 152.

[66] J. A. Hornbeck, J. R. Haynes, *Phys. Rev.* **1955**, *97*, 311.

[67] S. Ghatak, A. N. Pal, A. Ghosh, *ACS Nano* **2011**, *5*, 7707

[68] S. Ghatak, A. Ghosh, *Appl. Phys. Lett.* **2013**, *103*, 122103.

[69] W. Zhu, T. Low, Y.-H. Lee, H. Wang, D. B. Farmer, J. Kong, F. Xia, P. Avouris, *Nat. Commun.* **2014**, *5*, 3087.

[70] Z. Alaie, S. Mohammad Nejad, M. H. Yousefi, *Mater. Sci. Semicond. Process.* **2015**, *29*, 16.

[71] X.-M. Zhang, S.-H. Tseng, M.-Y. Lu, *Appl. Sci.* **2019**, *9*, 1110.

[72] K. Arora, N. Goel, M. Kumar, M. Kumar, *ACS Photonics* **2018**, *5*, 2391

[73] D. Akinwande, C. J. Brennan, J. S. Bunch, P. Egberts, J. R. Felts, H. Gao, R. Huang, J.-S. Kim, T. Li, Y. Li, K. M. Liechti, N. Lu, H. S. Park, E. J. Reed, P. Wang, B. I. Yakobson, T. Zhang, Y.-W. Zhang, Y. Zhou, Y. Zhu, *Extreme Mech. Lett.* **2017**, *13*, 42.

[74] J. F. Gonzalez Marin, D. Unuchek, K. Watanabe, T. Taniguchi, A. Kis, *npj 2D Mater. Appl.* **2019**, *3*, 14.

[75] Y. Wu, Z. Li, K.-W. Ang, Y. Jia, Z. Shi, Z. Huang, W. Yu, X. Sun, X. Liu, D. Li, *Photonics Res.* **2019**, *7*, 1127.

Supporting Information

Semimetal-Monolayer Transition Metal Dichalcogenides Photodetectors for

Wafer-Scale Ultraviolet Photonics

Hon-Loen Sinn,[1] Aravindh Kumar,[2] Eric Pop,[2,3,4] and Akm Newaz[1]

[1]Department of Physics and Astronomy, San Francisco State University, San Francisco, California 94132, USA

[2]Department of Electrical Engineering, Stanford University, Stanford, California 94305, USA

[3]Department of Materials Science and Engineering, Stanford University, Stanford, California 94305, USA

[4]Precourt Institute for Energy, Stanford University, Stanford, California 94305, USA

S1. Carrier dynamics

We calculated the photo-response using a modified Hornback-Haynes model,[1-5] in which the valence band has a tail by a distribution of states with density D_t and with energy $E_{v,t}$ above the valence band with Energy E_v. The photogenerated holes get trapped and de-trapped in those trap states near the valence band. Since our device is ON state due to the n-doping and as the Fermi energy is near the edge of the conduction band, we neglected the electron trapping. The recombination occurs via midgap states with an empirical (constant) rate $1/\tau_r$. We assumed that the recombination rate for both electrons and holes is the same. The holes are trapping into the states and de-trapping out of the states with a rate $1/\tau_t$ and $1/\tau_d$, respectively. We presented the physical mechanism schematically in Fig.S1.
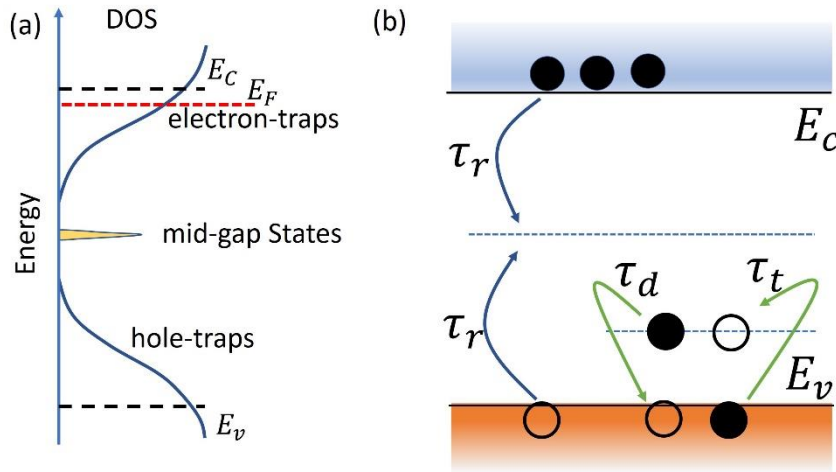

Figure S1: (a) Schematic illustration of the density-of-states (DOS) in 1L-MoS₂. The conduction band and valence band are at energy E_C and E_v, respectively. Band tail states exist underneath (above) the conduction (valence) band edge that act as electron (hole) charge traps. The recombination to occur via midgap states with an empirical (constant) rate $1/\tau_r$. We have assumed that the recombination rate for both electron and holes are the same. (b) Simplified energy band diagram that shows the main features of the charge trapping and detrapping model. The valence band trail is approximated by a discrete distribution of hole traps with density D_t (occupation of traps p_t). The holes are trapping into the states and de-trapping out of the sates with a rate $1/\tau_t$ and $1/\tau_d$, respectively.

Optical illumination creates carrier density in 1L-MoS₂. Because of charge neutrality, the change of carrier density due to optical illumination is given by,

$$\Delta n = \Delta p + p_t \tag{1}$$

where Δn (Δp) is the free electron (hole) concentration and p_t is the trapped hole carrier concentrations. The change in conductivity due to the optical illumination is given by,

$$\Delta \sigma = q(\mu_n + \mu_p)\Delta p + q\mu_n p_t \tag{2}$$

where $\mu_n(\mu_p)$ are the electron(hole) mobility and q is the electron charge. Hence the change in the conduction due to the presence of the traps is $q\mu_n p_t$.

Now, the equations for the carrier dynamics are given by,

$$\frac{d\Delta p}{dt} = \varphi - \frac{\Delta p}{\tau_r} + \frac{p_t}{\tau_d} - \frac{\Delta p}{\tau_t}\left(1 - \frac{p_t}{D_t}\right) \text{--------------(3)}$$

$$\frac{dp_t}{dt} = -\frac{p_t}{\tau_d} - \frac{\Delta p}{\tau_t}\left(1 - \frac{p_t}{D_t}\right) \text{--------------------(4)}$$

where φ is the absorbed photon flux and is given by $\eta P_D \lambda / hc$. Here η is the photon absorption coefficient, P_D is the optical power density, λ is the wavelength, h is the Planck constant, and c is the speed of light.

The steady-state condition allows us to set $\frac{d\Delta p}{dt} = \frac{dp_t}{dt} = 0$. By applying this steady condition, we obtain the following two equations.

$$\Delta p = \varphi \tau_r \text{--------------------(5)}$$

$$p_t = \frac{\varphi D_t \tau_t}{\varphi \tau_r + D_t\left(\frac{\tau_t}{\tau_d}\right)} \text{--------------(6)}$$

Since there is p_t holes are trapped, it creates an electrostatic voltage or gate voltage (ΔV_G), which we calculated using a simple capacitor model.

$$\Delta V_G = \frac{q p_t}{C} \text{------------------(7)}$$

where C is the effective capacitance and is given by,

$$\frac{1}{C} = \frac{1}{C_g} + \frac{1}{C_q}$$

where C_g is the geometrical capacitance and C_q is the quantum capacitance defined as $C_q = e2g_{2D}$. Here g_{2D} is the density of states of a 2D electron gas system and e is the electron charge.

We can calculate the photocurrent as

$$I_{PC} = \Delta V_G \frac{dI_{ds}}{dV_G} \text{------------(8)}$$

where $\frac{dI_{ds}}{dV_G}$ is the transverse conductance. By using Eq.8 and Eq.6, we can get

$$I_{PC} = \frac{q D_t}{C} \frac{dI_{ds}}{dV_g} \frac{1}{1 + \frac{D_t}{\varphi \tau_r}\left(\frac{\tau_t}{\tau_d}\right)} = A \frac{1}{1 + \frac{B}{P_D}} \text{----------(9)}$$

where two new parameters A and B are given by,

$$A = \frac{q D_t}{C} \frac{dI_{ds}}{dV_g}; \qquad B = \frac{D_t hc}{\eta \lambda \tau_r}\left(\frac{\tau_t}{\tau_d}\right) \text{----------(10)}$$

S2: Photoresponsivity of MoS2 devices with Schottky Au contacts

We studied CVD grown devices that are connected with Ag/Au electrical contacts. The devices were grown directly on a glass substrate. Figure S2 shows the optical image of one such device along with the photoresponsivity measured at 77 K. We observed that the photoresponsivity in Ti/Au connected device is six orders of magnitude lower than Bi- contacted device.
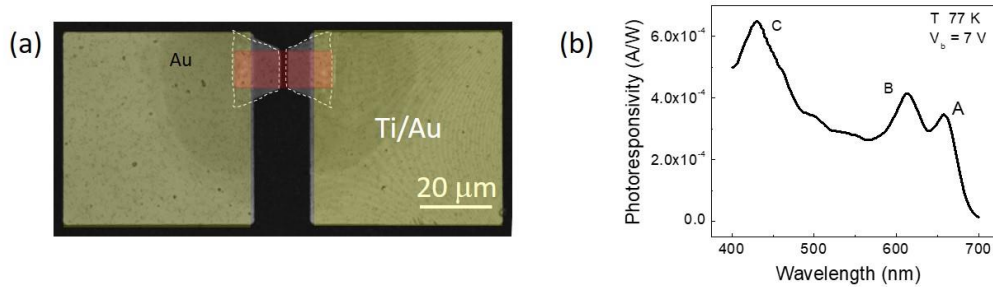

Figure S2: (a) The optical image (False-colored) of the sample. The 1L-MoS$_2$ etched ribbon is marked by a red rectangle. The Ag/Au (5/25 nm) electrical connection to the sample is marked by dashed trapezoid. (b) The photoresponsivity of sample measured at 77 K. The applied bias voltage was 9 V. We observed three peaks associated with the A-, B-, and C- excitons.

S3: Scanning photocurrent microscopy image

Scanning photocurrent image of a sample is shown Fig.S3. Since our sample resides inside a cryostat and we use a long working distance microscope objective (working distance ~ 17 mm), our laser beam diameter (~ 2 μm) is larger than the diffraction limited size. The scanning photocurrent image was measured at 77 K. We didn't observe any photocurrent outside MoS$_2$.
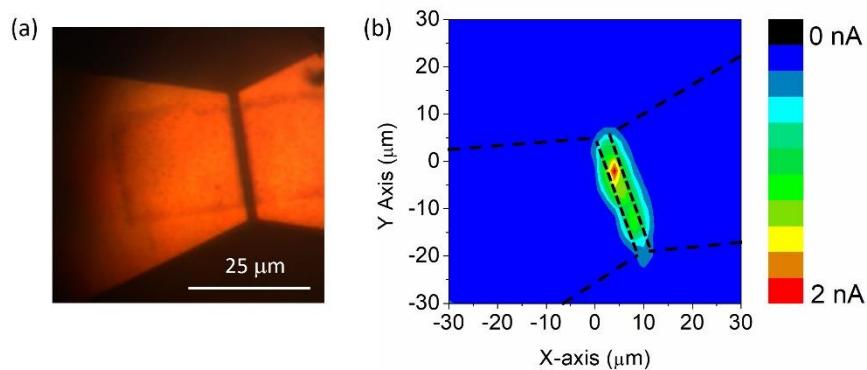

Figure S3: (a) The optical image of the sample used for the scanning photocurrent measurements. (b) The figure presents the scanning photocurrent measured at 77 K. The dashed black lines present the outline of the metal pads.

S4: Persistent photocurrent study

TMD based devices demonstrated persistent photoconductivity (PPC), which is sustained conductivity after illumination is blocked or removed.[6] The PPC in MoS2 has been attributed to the charge traps due to the inhomogeneities in the substrate. To investigate PPC, we have studied for 5 minutes after terminating the laser illumination as shown in Fig.S4. No persistent photocurrent was observed. Interestingly, we found that the dark current has some transient behavior whose origin is not currently known.
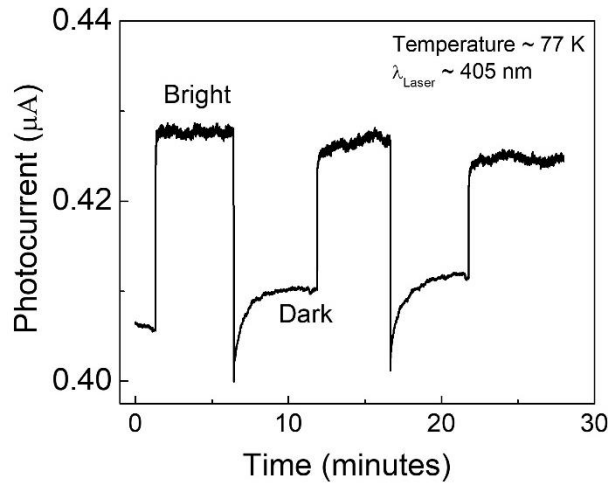

Figure S4: Photocurrent as we illuminate the sample and terminate the illumination. The measurement was conducted at 77 K. The photocurrent was measured by a digital multimeter (Keithley 2000).

References:

1. Furchi, M. M.; Polyushkin, D. K.; Pospischil, A.; Mueller, T. Mechanisms of Photoconductivity in Atomically Thin MoS$_2$. *Nano Letters* **2014**, 14, 6165-6170.
2. Macdonald, D.; Cuevas, A. Trapping of Minority Carriers in Multicrystalline Silicon. *Applied Physics Letters* **1999**, 74, 1710-1712.
3. Vaquero, D.; Clericò, V.; Salvador-Sánchez, J.; Díaz, E.; Domínguez-Adame, F.; Chico, L.; Meziani, Y. M.; Diez, E.; Quereda, J. Fast Response Photogating in Monolayer MoS$_2$ Phototransistors. *Nanoscale* **2021**, 13, 16156-16163.
4. Hornbeck, J. A.; Haynes, J. R. Trapping of Minority Carriers in Silicon. I. P-Type Silicon. *Physical Review* **1955**, 97, 311-321.
5. Fan, H. Y. Effect of Traps on Carrier Injection in Semiconductors. *Physical Review* **1953**, 92, 1424-1428.
6. Wu, Y.-C.; Liu, C.-H.; Chen, S.-Y.; Shih, F.-Y.; Ho, P.-H.; Chen, C.-W.; Liang, C.-T.; Wang, W.-H. Extrinsic Origin of Persistent Photoconductivity in Monolayer MoS$_2$ Field Effect Transistors. *Scientific Reports* **2015**, 5, 11472.